Geomorphology 500 (2026) 110229

Contents lists available at ScienceDirect

Geomorphology

journal homepage: www.journals.elsevier.com/geomorphology

Quantification of the active width in gravel-bed rivers: The effect of morphology, flood magnitude and survey frequency

Thomas G. Bernard [a,*], Enrico Pandrin [a], Lindsay Capito [b], Simone Bizzi [b], Walter Bertoldi [a]

[a] Department of Civil and Environmental Engineering, University of Trento, Trento, Italy
[b] Department of Geosciences, University of Padova, Padova, 35131, Italy

ARTICLE INFO

Keywords:
Active width
Sediment transport
Flume experiments
River morphology

ABSTRACT

Active width is a key indicator of bedload dynamics in gravel-bed rivers. While theoretical models typically refer to instantaneous bedload active width, its direct measurement in the field remains difficult due to high spatio-temporal variability. Consequently, morphological active width, derived from detectable bed changes after flood events, is often used as a proxy, though its relationship to bedload transport dynamics across different morphologies, flood magnitude, and survey frequencies remains poorly understood. This study aims to (a) quantify active width in relation to dimensionless stream power and morphology; (b) assess differences between bedload and morphological active widths across time intervals; and (c) evaluate the Exner timescale framework for linking transport dynamics to spatio-temporal morphological evolution. A physical model replicating braided, wandering, and alternate bar morphologies under controlled flow conditions, combining time-lapse imagery and DEM differencing, was used to address these objectives. Results were compared with field data from the Tagliamento (Italy), Rees (New Zealand Aotearoa), and Sunwapta (Canada) rivers. Findings show a strong correlation between active width and dimensionless stream power and reveal a large effect of the timespan, ranging from 0.4 to 3 times the Exner timescale. Morphological active width was consistently lower than the time-integrated bedload active width, with larger differences for single-thread/wandering morphologies, reaching 33%, compared to braiding (about 10%) and remaining constant with increasing timespan. Comparison with repeated DEMs of Difference (DoDs) in the field confirmed the validity of the approach, with both dimensionless stream power and the timespan between surveys controlling the morphological active width.

1. Introduction

Bedload transport in gravel-bed rivers is highly variable in space and time, both in terms of occurrence and magnitude, responding dynamically to changes in flow conditions. Understanding this response for various river morphologies is fundamental for predicting sediment transport rates and channel evolutionary trajectories, but still represents a notorious challenge in fluvial geomorphology (Ancey, 2020a, 2020b and references therein). Yet, a deeper understanding of the dynamics of these processes is essential to improve predictions and to support effective river management, including flood risk mitigation (Vázquez-Tarrío et al., 2024), habitat restoration, and the preservation of ecological functions (Wohl et al., 2015, 2024; Williams et al., 2016; Piégay et al., 2023).

While direct field measurements of bedload flux remain challenging due to its spatial heterogeneity and temporal variability, the active width - the lateral extent of bed material displacement over time - has emerged as a meaningful and measurable proxy for bedload transport dynamics (Brenna et al., 2022). Field and laboratory observations have shown that active width expands and contracts with discharge, directly influencing bedload transport (Davoren and Mosley, 1986; Ferguson et al., 1992; Haschenburger and Church, 1998; Haschenburger and Wilcock, 2003). Moreover, in gravel-bed rivers, bedload transport occurs in narrow, discontinuous areas along the channel network, with changes in the active width serving as the primary response to flow variations (Bertoldi et al., 2009a; Ashmore et al., 2011). Flume and field observations indicate that the active width can be as little as 10–15% of the wetted width and generally no more than 50% in braided rivers. Flume experiments further confirm a strong correlation between active width and sediment transport rates, particularly in braided systems, where active width is linked to active braiding intensity (ABI) and sediment bulk changes (Egozi and Ashmore, 2009; Peirce et al., 2018).

* Corresponding author.
E-mail address: thomas.bernard@unitn.it (T.G. Bernard).

https://doi.org/10.1016/j.geomorph.2026.110229
Received 2 September 2025; Received in revised form 13 February 2026; Accepted 14 February 2026
Available online 20 February 2026

Beyond its role in transport dynamics, active width shows strong positive correlations with easily measurable parameters from field data, such as wetted width and stream power (Bertoldi et al., 2009a; Garcia Lugo et al., 2015; Middleton et al., 2019). These results proved that active width can serve as a useful parameter to estimate sediment flux and to model river evolution across different flow regimes. Peirce et al. (2018) also suggest that, when combined with other metrics, active width could provide useful insights for distinguishing between different river types.

However, the interpretation and the prediction of active width remain challenging due to variations in its conceptualization across different spatial and temporal scales of observation, partly due to different measurement techniques (Ashmore et al., 2011). Three distinct concepts of active width exist: the instantaneous bedload active width, the morphological active width, and the active channel width, or active corridor width. The instantaneous bedload active width represents the channel section actively transporting bedload at a given moment (Garcia Lugo et al., 2015). The morphological active width quantifies the areas where sediment deposition and erosion occur over a defined period (typically days to years, encompassing one or more transport events), as obtained from repeated riverbed surveys (Ashmore et al., 2011; Peirce et al., 2018). The active channel width, or active corridor width, is defined by the extent of water and unvegetated bars, capturing long-term channel adjustments over years to decades and usually mapped from remotely sensed data, e.g. aerial or satellite imagery (Williams and Rust, 1969; Liébault and Piégay, 2002; Belletti et al., 2015; Brenna et al., 2022). While the timeframe for the instantaneous active width is well defined, the timescales of measurements for the other two approaches vary significantly, adding complexity to interpretation and comparison.

One major source of uncertainty is the lack of a clear link between instantaneous bedload transport, its time-integrated spatial pattern, and the resulting morphological changes. While sediment transport models often rely on instantaneous fluxes, active width measurements are typically time-integrated, making it difficult to determine the optimal temporal scale for capturing transport dynamics, if there is any. In braided rivers, it is expected that active width approximates instantaneous flux predictions at sufficiently short intervals (Lindsay and Ashmore, 2002) but this has never been systematically quantified, nor has its validity been assessed across different river morphologies due to challenges in characterizing the spatial distribution of the instantaneous bedload transport. Ashmore et al. (2011) pointed out that “the answer to this question will provide some insight into rates of bed elevation change and the way in which spatial patterns of instantaneous flux result in morphological change” for various morphologies of gravel-bed rivers. Additionally, the relationship between morphological and bedload active widths remains unclear, particularly how this relationship evolves with the increase of the time interval between consecutive surveys. Another key challenge is the absence of a standardized approach for analyzing and comparing active width measurements across studies. Since the active width depends not only on the time interval between surveys but also on the frequency, magnitude, and duration of flood events during this period, integrating flow history into its analysis is essential. Developing a systematic method that accounts for these factors, regardless of the measurement technique used, would enhance comparability and improve predictions of bedload transport response to flow conditions.

Because of the difficulty in capturing bedload transport patterns over time in the field, physical and numerical models remain the most effective tools for analyzing the relationship between bedload transport and morphological change (Javernick et al., 2018; Bakker et al., 2019). Recent advances in remote sensing techniques in physical modelling have significantly improved the ability to map bedload transport over time with unprecedented spatiotemporal resolution. Redolfi et al. (2017) introduced a time-lapse imagery approach that detects bed variation due to grain displacement using a fixed camera, and this method has been shown to accurately capture instantaneous bedload transport patterns and intensity (Javernick et al., 2018). However, its potential for analyzing the spatiotemporal dynamics of bedload transport in response to varying flow conditions and river morphologies remains largely unexplored.

This study integrates these approaches to investigate the variability and relationships between instantaneous bedload active width, time-integrated bedload active width, and morphological active widths across different timescales of topographic survey acquisitions, flow characteristics, and river morphologies. Specifically, it aims:

a. to characterize the instantaneous active width in relation to river morphology and dimensionless stream power;
b. to assess how bedload and morphological active widths differ across time intervals and river morphologies;
c. and to evaluate whether the timescale framework based on the sediment mass conservation equation (Exner, 1925; Garcia Lugo et al., 2015) offers a consistent and reliable basis for quantifying morphological changes across different transport events and river morphologies.

To achieve this, a physical model of gravel-bed rivers developed at the University of Trento is used to replicate various river morphologies under controlled flow conditions, enabling continuous spatial and temporal monitoring of bedload transport and morphological changes, using a Digital elevation model (DEM) differencing approach. The experiments generated high-resolution maps of bedload transport activity and its morphological imprint across five channel-forming discharges, capturing river morphologies ranging from alternate bars to braided. The laboratory findings were compared to repeated topographic surveys of a braided reach of the Tagliamento River (Italy) and through the comparison with previously published data on the Rees River (New Zealand Aotearoa, Brasington et al., 2012; Williams et al., 2014) and the Sunwapta River (Canada, Ashmore et al., 2011).

2. Methodology and data

2.1. Flume experiments

The experiments were performed in a 24 m long and 0.6 m wide flume at the University of Trento, Italy. The flume's longitudinal slope (S) was set to 0.01 m/m and the corridor area – the area between the two banks - has been filled with uniform sand with a median grain size (D_{50}) of 1 mm (Fig. 1). The setup of the experiments was designed to reproduce hydraulic and morphological conditions representative of gravel-bed rivers, rather than to replicate a specific river prototype. Experimental conditions were chosen to ensure turbulent flow in the sediment-transporting zones (Reynolds number > 4000) and to maintain bedload-dominated transport, with cross-sectional average Shields stresses between 0.04 and 0.18. The resulting depth-to-grain-size ratios ranged from 7 to 30, consistent with those typically observed in gravel-bed rivers (Powell, 2014; Garcia Lugo et al., 2015).

At the upstream end, the input water discharge Q was regulated using a pump controlled by an electromagnetic flow meter. The sediment supply was provided by a calibrated sand feeder and adjusted according to the water discharge to keep an overall equilibrium between sediment input and output. At the downstream end, a chute collected the output water and sediment fluxes. The output sediment flux was estimated from the cumulative weight of the collected material in a submerged tank equipped with load cells, with a resolution of 100 g and a sampling interval of 10 s.

Two Nikon D7100 cameras were used to record sediment transport, one fitted with an AF-S NIKKOR 18–55 mm f/3.5–5.6G VR II lens and the other with an AF-S NIKKOR 18–55 mm f/3.5–5.6G ED lens. Both cameras were set to a shutter speed of 1.3 s, ISO 100, aperture f/5.6, saturation 0, and cool-white fluorescent white balance (4200 K) to ensure consistent color representation and minimal noise. These settings

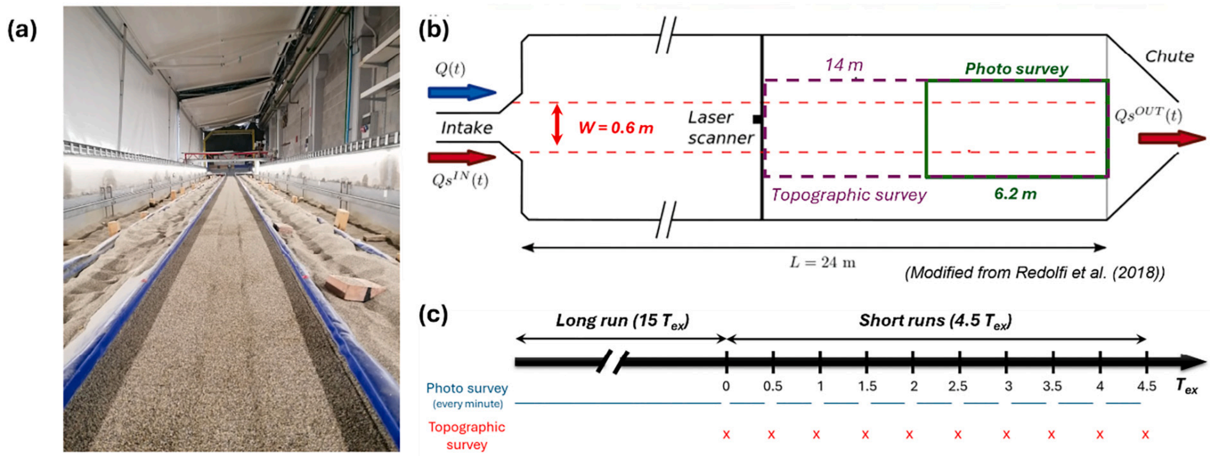

Fig. 1. (a) Photograph of the flume configuration with a downstream view. (b) Schematic representation of the flume settings where Q is the input water discharge, Q_s^{IN} and Q_s^{OUT} the input and output sediment flux respectively (modified from Redolfi et al. (2018)). (c) Sketch of experimental design. T_{ex} refers to the Exner timescale (see Eq. (1)).

optimized dynamic range and exposure while allowing sediment-induced changes in image saturation to be accurately captured for quantitative analysis. Time-lapse imagery was captured of the final 6.2 m of the flume at approximately 1 mm resolution, providing the database for bedload transport mapping (see Section 2.2). To prevent light disturbances in the photos, the flume was covered with lighting provided by two LED strips mounted along the external walls. A laser scanner (M5L/200 by Mikroelektronik GmbH), with an accuracy of 0.1 mm, was used to repeatedly monitor bed elevation, with a grid spacing of 50 mm in the longitudinal direction and 5 mm in the transverse direction. Topographic surveys were conducted over the last 14 m of the flume to avoid upstream boundary effects. Before each experiment, a narrow rectangular channel, 0.15 m wide and 0.01 m deep, was created at the center of the corridor to facilitate channel bed development.

Five experiments were performed using constant channel-forming water discharges of 0.5, 0.7, 1.0, 1.5, and 2.0 l/s, each paired with an input sediment flux adjusted to maintain equilibrium with the output flux (Table 2). The experiments are labeled according to formative discharge as q05, q07, q10, q15, and q20. The q05 experiment allows exploration of near-threshold sediment transport conditions. The duration of each experiment was set based on the flow and sediment transport conditions, to guarantee a normalized timescale across all experiments. We followed the approach proposed by Garcia Lugo et al. (2015), using the timescale derived from the sediment mass conservation equation (Exner, 1925), such that the volume of sediment transported in each run remains comparable under varying conditions (see also Capito et al., 2024; Fujita, 1989). This timescale, hereafter referred to as the Exner timescale T_{ex}, is expressed as:

$$T_{ex} = (1-p)\frac{D \bullet W_w^2}{Q_s^{OUT}} \tag{1}$$

where p is the sediment porosity, D the mean water depth, W_w the mean wetted width and Q_s^{OUT} the mean output volumetric sediment flux. In the following, we denote the normalized time variable as T_{ex}^*, defined as the ratio between dimensional time and the Exner timescale.

The experimental procedure was designed to compare bedload transport planform activity with its resulting morphological imprints, while maintaining a reasonably short duration to permit multiple experiments. The experimental procedure, summarized in Fig. 1c, followed several steps. First, a long run lasting approximately 15 times T_{ex} (i.e., a normalized time interval $\Delta T_{ex}^* = 15$) was conducted to ensure full reworking of the corridor area and the development of a near-equilibrium morphological state. A second long run of the same duration followed, during which a photographic survey was conducted at a rate of one photo per minute, and the output sediment flux was measured. After this phase, the riverbed was dried and surveyed. The final phase of each experiment consisted of nine short runs, each lasting 0.5 times T_{ex} $(\Delta T_{ex}^* = 0.5)$, with similar photographic monitoring. The choice of nine runs and their duration ensured sufficient measurable morphological change while limiting compensation processes and keeping the total experimental duration (run time plus laser survey) manageable. Between each short run, the water flow was stopped, and the dry riverbed was surveyed (Fig. 1c). It is important to note that while an initial estimate of the Exner timescale was used to design the experiment durations, the analysis is based on a refined computation, using average values of the relevant parameters over each entire run. As a result, the final T_{ex} values differ slightly from the initial estimate and therefore the final normalized time durations of the runs are not exactly 0.5 (see Section 3.1).

2.2. Mapping of bedload transport and morphological changes

To map the spatiotemporal variability of bedload transport, the time-lapse imagery technique developed by Redolfi et al. (2017) was used. This method detects multiple grain displacements within a region by analyzing macroscopic differences in the saturation band between successive images, with the magnitude of these differences assumed to correlate with bedload transport intensity. Further details on the technique can be found in Redolfi et al. (2017).

The processing workflow begins with merging images from the two cameras and computing saturation differences. Details on the image processing procedure can be found in the Supplementary materials (Section S1). An image analysis procedure then filters out noise caused by shadows from the flume banks and light reflections on the water surface (present only for the two highest discharges), through automated detection of shadowed and blurry regions based on intensity averaging, Gaussian smoothing, thresholding, and morphological operations. The procedure was implemented in Python using functions from the *SciPy* and *scikit-image* libraries (Van Der Walt et al., 2014; Virtanen et al., 2020). The resulting masks remove spatially coherent dark areas and regions lacking high-frequency texture. Next, a spatial averaging step is applied using a 0.011 m × 0.011 m moving window, followed by a thresholding process to identify regions where sediment transport occurs. The saturation threshold was calibrated based on visual inspection of consecutive images and was similar between experiments, ranging from 5.7 to 7 over values of 0 to 255. Finally, morphological image analysis using *SciPy*, *scikit-image* and *OpenCV* python libraries

(Bradski, 2000), is applied to the thresholded difference images to remove areas likely not associated with active bedload transport. This procedure uses erosion, hole filling, neighborhood filtering, and connected-component analysis to retain only spatially coherent and persistent regions. It suppresses illumination artefacts, optical blur, static background patterns, and small isolated features, ensuring that subsequent measurements rely solely on physically meaningful transport signals.

Morphological changes were mapped by subtracting two consecutive DEMs, thus obtaining DoD maps, and applying a three-step filtering process to remove noise from surface roughness and measurement inaccuracies. First, a three-point moving average was applied along the transverse direction. Second, a uniform 0.0013 m detection threshold (i.e., slightly larger than the grain size) was applied, setting lower values to zero to remove most of the noise. Then, small, isolated features (one or group of cells) were iteratively removed, and minor gaps within clusters were filled using morphological operations (*scipy.ndimage*, *skimage.morphology*) to preserve spatially coherent regions. Additional neighborhood and filtering in the transversal direction (finnest spatial resolution) removed residual artefacts, resulting in DoDs that retained only contiguous, persistent regions corresponding to genuine sediment transport. More details can be found in Capito et al. (2024).

The final dataset consists of two sets of maps: the first represents the 2D spatial distribution of bedload transport activity at one-minute intervals, while the second illustrates both the 2D spatial distribution and magnitude of morphological changes at approximately 0.5 T_{ex} intervals. This dataset provides the highest temporal resolution in survey frequency for both bedload transport and morphological evolution. To analyze these processes across different timescales, cumulative maps, referred to as "envelope" maps, were generated to describe the total area of bedload transport activity over a given period. Moreover, to analyze the effect of the timespan between survey acquisitions, DoD maps were also computed for non-consecutive DEMs, increasing the time interval ΔT^*_{ex} from the minimum value of approximately 0.5 to a maximum value of approximately 4.5 (i.e., the interval between the first and last survey of each run). An example of the different maps is shown in Fig. 2.

2.3. Tagliamento, Rees and Sunwapta rivers data

To support the laboratory results, data from three different gravel-bed braided rivers were analyzed: the Tagliamento River (Italy), the Rees River (Aotearoa New Zealand) and the Sunwapta River (Canada). For these case studies, sequences of repeated DEMs accompanied by detailed hydrological data were available (Ashmore et al., 2011; Brasington, 2010; Capito, 2024).

The study reach of the Tagliamento River is located south of Pinzano village, extending 1 km in length and approximately 570 m in width. It features a braided morphology, with a riverbed slope of 0.003 m/m and a median grain size of 0.028 m. Water discharge was estimated from flow level recorded at the Venzone gauging station, approximately 27 km upstream, using an available stage-discharge rating curve (Bertoldi et al., 2010). Based on field observations and numerical modelling, Bertoldi et al. (2010) estimated that the critical discharge for initiating bedload particle motion is approximately 150 m^3/s. Over a three-year period, five topographic surveys were conducted at low flow, using UAV-based (Unmanned Aerial Vehicule) acquisition in February and September 2021, January and November 2022, and June 2024. The UAV images were processed to obtain DEMs with a grid resolution of 1 m, where the bathymetry was estimated from the red-over-green bands ratio (Legleiter et al., 2004) of the 0.5 m orthoimages, a method previously applied on the same river (Bertoldi et al., 2011). During this period, one major flood event with approximately 20-year return interval occurred in November 2023, along with three minor floods in November 2021, April 2024 and May 2024. Six intermediate floods also occurred, with at least one between each pair of surveys, leading to significant morphological changes. These changes were quantified using a DEM of differences technique (DoD) approach, following the recommendation of Wheaton et al. (2010) to define error thresholding. Error thresholding in DoD was applied by first estimating individual DEM errors using GCPs, then propagating these into the DoD using a standard deviation-based formula. A probabilistic thresholding approach was used to assess the significance of elevation changes, applying a user-defined confidence interval based on the propagated uncertainty. A uniform propagated error of 15 cm was used across all DoDs, derived using a weighted average to account for higher errors in submerged areas (more details on the survey acquisition strategy and processing can be found in the Supplementary materials Section S2 and in Capito (2024)).

The Rees River is a large braided river in the Southern Alps of New Zealand that has been extensively studied in recent years (Williams

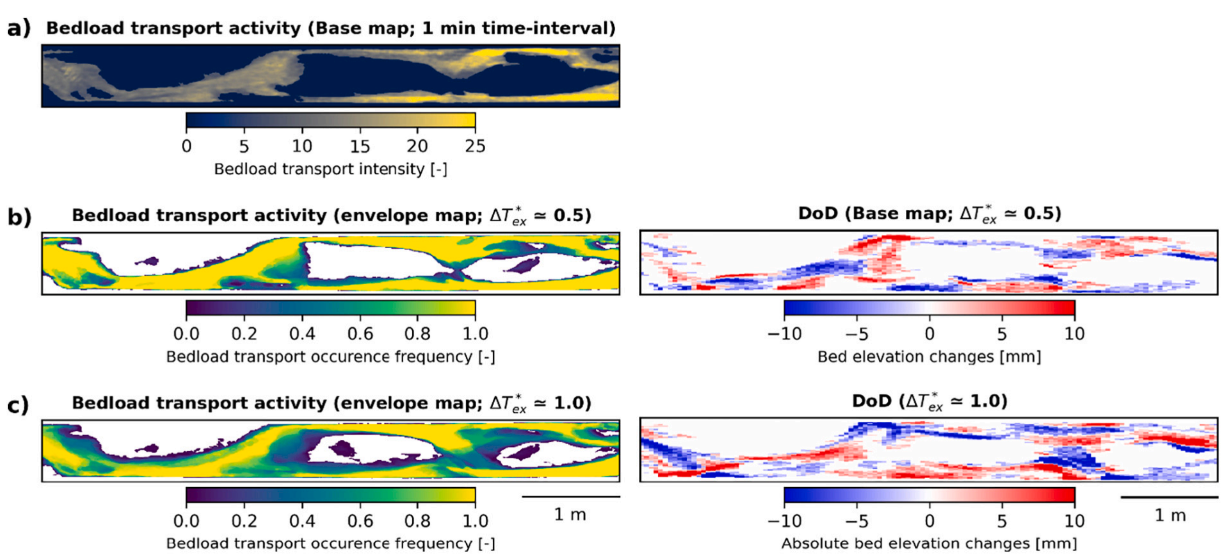

Fig. 2. Examples of instantaneous and time-integrated bedload transport activity and DoD maps at Exner time-interval $\Delta T^*_{ex} \approx 0.5$ and $\Delta T^*_{ex} \approx 1$. a) Instantaneous bedload transport activity map with transport intensity. b) Bedload transport activity frequency map and corresponding DoD for $\Delta T^*_{ex} \approx 0.5$. c) Same as b) for $\Delta T^*_{ex} \approx 1.0$. Bedload transport activity maps represent cumulative transport envelopes over a given Exner time-interval while DoDs are derived from DEMs separated by the respective Exner timespans. Maps were produced based on short-runs from the q10 experiment.

et al., 2014). The monitored reach is 2.5 km long, about 800 m wide, with a riverbed slope of 0.0057 m/m and a median grain size of 0.02 m. As reported by Brasington (2010) and Williams et al. (2014) eight topographic surveys were conducted using terrestrial LiDAR before and after 10 sequential flood events between October 2009 and May 2010. Discharge data were estimated from water levels recorded every 15 min at a gauging station located a few km upstream, where the confined, single-thread channel allowed for calibration of a flow-stage relationship. Redolfi et al. (2016) estimated the sediment transport threshold at approximately 30 m^3/s, based on field observations of morphological change. During the survey period, discharge varied between 100 and 350 m^3/s, including a 10-year return interval event. High-resolution DEMs with a 0.5 m grid were created by combining topographic LiDAR data with bathymetric estimates obtained using optical techniques similar to those used in the previous case study. Details on point cloud processing and bathymetric reconstruction can be found in Williams et al. (2014).

The Sunwapta River is a gravel-bed pro-glacial river draining the Athabasca Glacier in Jasper National Park, Alberta, Canada. Data from Ashmore et al. (2011) were used, focusing on a 150 m long reach and about 100 m wide, characterized by a longitudinal slope of 0.0132 m/m and an average grain size of approximately 0.04 m. Discharge was estimated from stage measurements immediately upstream, using a calibrated stage-discharge relationship. The maximum observed discharge was 14.1 m^3/s, corresponding approximately to bankfull conditions. Ten cross-sections spaced 10–12 m apart were surveyed daily during the 2003 melt season, resulting in 12 repeated topographic surveys. Of these, five showed minimal morphological change, and two others were associated with flows high enough to induce significant change. The sediment transport threshold was estimated at approximately 12 m^3/s.

2.4. Active widths calculation and the Exner timescale framework

Bedload and morphological active widths were derived from bedload transport and morphological changes maps respectively. In this paper, active widths were calculated by dividing the active area by the reach length and were normalized by the maximum wetted width, and thus refer as active width ratios:

$$W_b = \frac{A_{bedload}}{L_{reach}.W_w} \times 100, \tag{2a}$$

$$W_m = \frac{A_{morphological\ changes}}{L_{reach}.W_w} \times 100, \tag{2b}$$

where W_b and W_m are bedload and morphological active width ratios, respectively, $A_{bedload}$ and $A_{morphological\ changes}$ are the active areas, as observed from the timelapse images and from the detected morphological changes areas from the DoDs, L_{reach} the reach length and W_w the wetted width.

For the three field case studies, the Exner timescales for each DoD

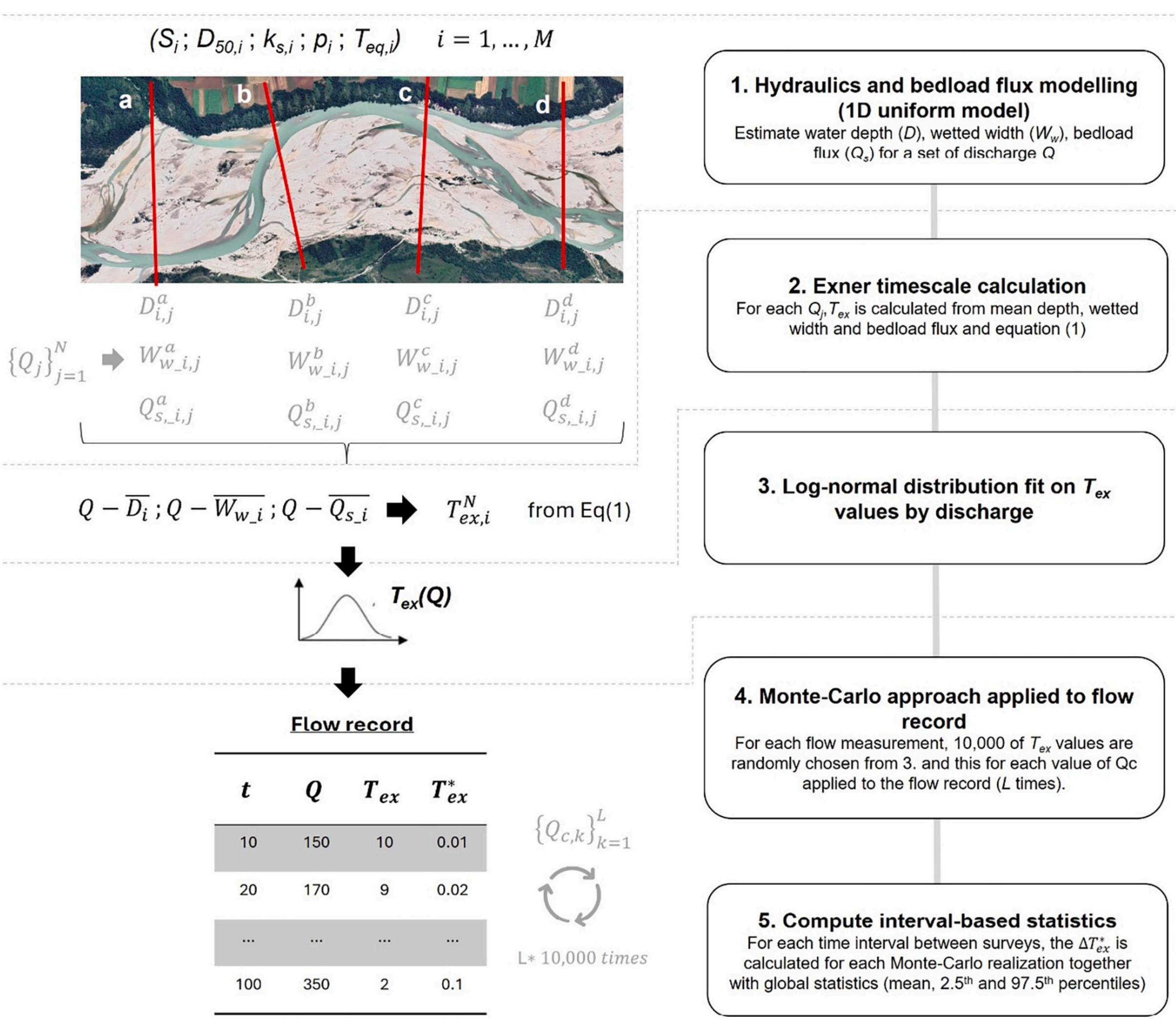

t	Q	T_{ex}	T^*_{ex}
10	150	10	0.01
20	170	9	0.02
...	...	...	...
100	350	2	0.1

Fig. 3. Workflow of the Exner timescale framework applied to field-based data.

(Eq. (1)) were derived from available flow records, and mean reach-scale water depth, wetted width, and bedload flux were estimated using one-dimensional numerical modelling. Uncertainties in the resulting Exner timescales were quantified using a Monte Carlo approach similar to Recking et al. (2024) (Fig. 3). The main steps are summarized as follows:

1. Establishment of discharge–variable relationships (step 1). Average reach-scale relationships between discharge and key variables (water depth, wetted width, and bedload flux) were established for a range of input parameter values (Table 1), with each parameter set defining a model run. This was achieved using a 1D uniform flow model applied to high-resolution cross-sectional data following Bertoldi et al. (2009a). The Tagliamento cross-sections were extracted from the UAV-derived DEMs with bathymetry (see Section 2.3). The same 1D model was used to compute the mean water depth for the laboratory experiments. Bedload fluxes were estimated using both the Parker (1990) and Wong and Parker (2006) formulations, selected for their previously demonstrated consistency in gravel-bed rivers (Bertoldi et al., 2009a; Redolfi, 2014).
2. Computation of reach-scale Exner timescales by discharge (step 2 and 3). For each model run, the Exner timescales were computed over a range of discharges based on previously discharge-depth, discharge-width, and discharge-bedload flux relationships together with Eq. (1). Given the range of parameters investigated (Table 1), this resulted in a dataset of 162 values of T_{ex} by discharge for each study site. Each dataset was subsequently fitted with a log-normal probability distribution.

Monte Carlo integration over flow records (step 4 and 5). The Exner time interval ΔT^*_{ex} associated with each flood event and with the period between topographic surveys was computed based on the site-specific flow records. A Monte Carlo approach was applied to estimate T_{ex} and the Exner timescale ratio T^*_{ex} (i.e., the actual time interval between measurements divided by the Exner timescale) for each time step of the flow record and to quantify the uncertainty following Recking et al. (2024) approach. For each discharge measurement, 10,000 values of T_{ex} were randomly sampled from the fitted log-normal distribution and T^*_{ex} were subsequently calculated. Then, flood events were identified when discharge Q exceeded the critical threshold discharge Q_c for sediment transport (i.e., $Q > Q_c$). To account for uncertainty in Q_c, the Monte-Carlo procedure was repeated for three different Q_c values (Table 1), resulting in a total of 30,000 T_{ex} and T^*_{ex} values per discharge measurement. The Exner time interval ΔT^*_{ex} was then computed as the cumulative sum of T^*_{ex} over each flood event and between successive surveys. The mean and the 2.5th and 97.5th percentiles were then calculated. In addition, the reach-scale maximum wetted width and the mean dimensionless stream power (ω^*) were computed, with ω^* as:

Table 1
Summary of the investigated range of parameters to estimate hydraulics, sediment fluxes and the uncertainty related to the Exner timescale calculations.

	Rees	Tagliamento	Sunwapta
Mean slope [–]	0.0057 ± 10%	0.003 ± 10%	0.013 ± 10%
Median grain size D_{50} [m]	0.020 ± 20%	0.028 ± 20%	0.060 ± 20%
Manning conveyance coefficient $1/n$ [$m^{1/3}/s$]	40.0 ± 20%	30.0 ± 20%	23.5 ± 20%
Porosity [–]	0.30 ± 20%	0.30 ± 20%	0.20 ± 20%
Bedload transport equation	Parker (1990), Wong and Parker (2006)[a]	Parker (1990), Wong and Parker (2006)	Parker (1990), Wong and Parker (2006)
Critical discharge Qc [m^3/s]	20; 30; 40	140; 150; 160	11; 12; 13

[a] With grain size classes used in Redolfi (2014).

Table 2
Resulting data from the experimental runs.

Run name	q05	q07	q10	q15	q20
Q [l/s]	0.5	0.7	1.0	1.5	2.0
Total long run duration [h]	20.8	15.0	6.8	6.2	7.3
Short run duration [min]	95	47	25	19	15
Output sediment flux $Qs_{out} \pm \sigma$ [g/s]	0.15 ± 0.12	0.33 ± 0.18	0.78 ± 0.30	2.39 ± 0.78	3.34 ± 0.97
Wetted width [m]	0.51	0.54	0.58	0.59	0.6
Mean water depth [m]	0.007	0.008	0.010	0.012	0.014
Wetted width/ corridor width	0.85	0.9	0.97	0.99	1
Instantaneous Active width/ corridor width	0.14	0.25	0.43	0.54	0.65
Dimensionless stream power ω^*	0.07	0.09	0.13	0.19	0.24
Exner timescale T_{ex} [min]	208	132	73	32	28
Planform style	Braided	Braided	Braided	Wandering	Alternate bars

$$\omega^* = \frac{Q.S}{W_w\sqrt{g\Delta_\rho D_{50}^3}}, \tag{3}$$

where g is the acceleration due to gravity and Δ_ρ the relative submerged sediment density. The dimensionless stream power is used to compare the results of active widths across various flow conditions and parameter scales (Bertoldi et al., 2009a, 2009b; Garcia Lugo et al., 2015).

3. Results

3.1. Flume experiments

3.1.1. River morphologies, output bedload fluxes, hydraulics, and Exner timescales

Mean values of the main parameters for each laboratory experiment are reported in Table 1, with the average output sediment flux measured during the long runs. The reach-scale average wetted width decreases from the full corridor width (0.6 m) in the q20 experiment to 0.51 m in the q05 experiment, marking a transition from a morphology characterized by fully submerged alternate bars to wandering and braiding morphologies. Planform style was classified using visual counting of the number of channels and the dominant morphological processes.

In the q20 experiment, submerged bars migrate slowly downstream, occasionally interrupted by chute cutoffs. As the dimensionless stream power decreases, the mean wetted width contracts from the full corridor width, exposing bar tops. This leads to more frequent chute cutoffs, promoting greater channel branching and increased morphological complexity in the final riverbed. The river morphologies thus range from wandering (q15 experiments) to a braided pattern with an increasing area of exposed sediments and reduced relief of scours and bar tops, in q10, q07 and q05 (Fig. 4).

Based on the experimental results, the Exner timescales were refined from the initial estimates used in the experiment design and found to be longer (by around 40% for q07 and q10 runs and < 20% for q15 and q20 runs). The final Exner timescales ranged by nearly an order of magnitude, from 208 min at the lowest discharge to 28 min at the highest, primarily reflecting differences in sediment flux.

3.1.2. The instantaneous bedload activity and active width

Details on the instantaneous bedload active area dynamics can be

Table 3
Statistics for the instantaneous W_b from long runs, time-integrated W_b and W_m from short runs.

	Run name	q05	q07	q10	q15	q20
Instantaneous W_b [%]	**n**	1040	660	365	160	140
	Min	10.6	20.3	37.2	50.0	58.8
	Max	24.4	33.7	54.9	59.5	71.9
	Mean	16.6	28.0	44.1	55.0	65.3
	Std	2.4	2.5	2.6	2.7	3.0
	CV	0.145	0.090	0.059	0.049	0.046
Time integrated W_b [%]	**n**	9	9	9	9	9
	T^*_{ex}	0.41	0.32	0.27	0.49	0.37
	Min	28.2	38.1	53.2	51.6	74.1
	Max	48.5	48.4	63.1	75.9	82.4
	Mean	36.7	43.9	58.4	65.7	80.1
	Std	6.6	3.2	3.5	8.8	2.5
W_m [%]	**n**	9	9	9	–	9
	T^*_{ex}	0.46	0.37	0.34	–	0.56
	Min	21.3	24.5	32.8	–	43.4
	Max	33.4	32.8	38.3	–	51.1
	Mean	27.8	28.5	35.2	–	47.3
	Std	4.2	2.7	2	–	2.4

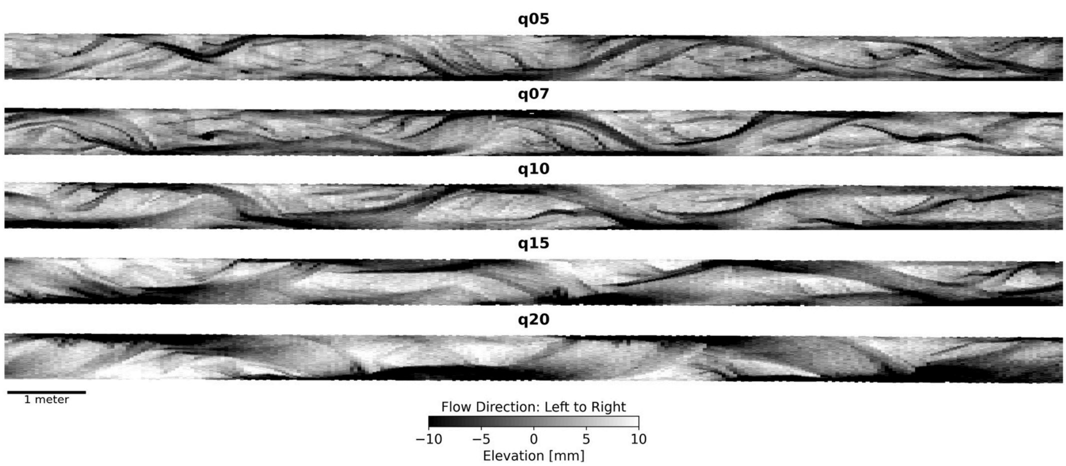

Fig. 4. Relative elevation model of the resulting river morphologies at the end of each long-run. Each REM is slope-corrected, and the elevation is relative to the mean elevation.

highlighted by the frequency map (i.e. the number of times a pixel was considered as active bedload transport divided by the total time) and by a snapshot of it (Fig. 5). The evolution of active channels across different flow conditions reveals a progressive shift from a well-connected, single-active channel system to a more fragmented and dynamic active channel network.

In the q20 experiment, a single, well-connected permanent active channel (activity frequency > 0.9) dominated the corridor over the entire experiment duration, with no fixed bars and full-width reworking of the riverbed. Bars migrated downstream and laterally from the margins toward the center by occasionally chute-cutoffs, forming a temporary secondary small active channel. At q15, a central bar emerged alongside lateral bars, marking the onset of increased morphological complexity. The q10 experiment displayed unstable active channel configurations and the onset of discontinuous active channels, with significant lateral migration and frequent avulsions. Intermittent active areas (0.3 < activity frequency < 0.7) are larger than other experiments representing 45% of the total active area compared to <26% for the other experiments. For about half of the experiment's duration, two active channels coexisted, one positioned near the left bank and the other near the right bank of the corridor. In the q07 experiment, a single, continuous active channel dominated, though transitional phases with two instantaneous channels occasionally occurred. An instantaneous snapshot revealed an upstream shift of the active channel from the center to the left bank, triggering a corresponding downstream transition in bedload transport and channel connectivity. Finally, the q05 experiment exhibited the most disconnected channel configuration in which permanent active areas represent only 3.3% of the total active areas while intermediate to low frequency areas (activity frequency < 0.7) represent 93%. A snapshot captured an avulsion from an upper active channel to a newly formed lower-right channel, which persisted for the final 4.5 h of the experiment. This highlights the increasing fragmentation and complexity of active channel patterns under lower flow conditions.

Results show that the reach-scale instantaneous W_b increases with ω^* from 16.6% for the q05 experiment to 65.3% for the q20 (Fig. 6a and b). Furthermore, the reach-scale instantaneous W_b fluctuated during each experiment duration with a trend in the magnitude of this variability in function of ω^*. The coefficient of variation *CV* increases with the decrease of ω^* from 0.145 for the q05 experiment to 0.046 for the q20 experiment (Table 3).

3.1.3. The morphological active width

This section presents the mean and the variability of the reach-scale morphological active width W_m as a function of the normalized Exner timescale ratio T^*_{ex} and dimensionless stream power ω^* (Fig. 7). The mean W_m was calculated for each experiment over nine measurements at the highest temporal resolution, here around 0.4 T_{ex} (Table 3). Examples of DoDs produced at a time interval ΔT^*_{ex} of around 0.4 are presented in Fig. 8b. Issues in the input water discharge during the q15 experiment

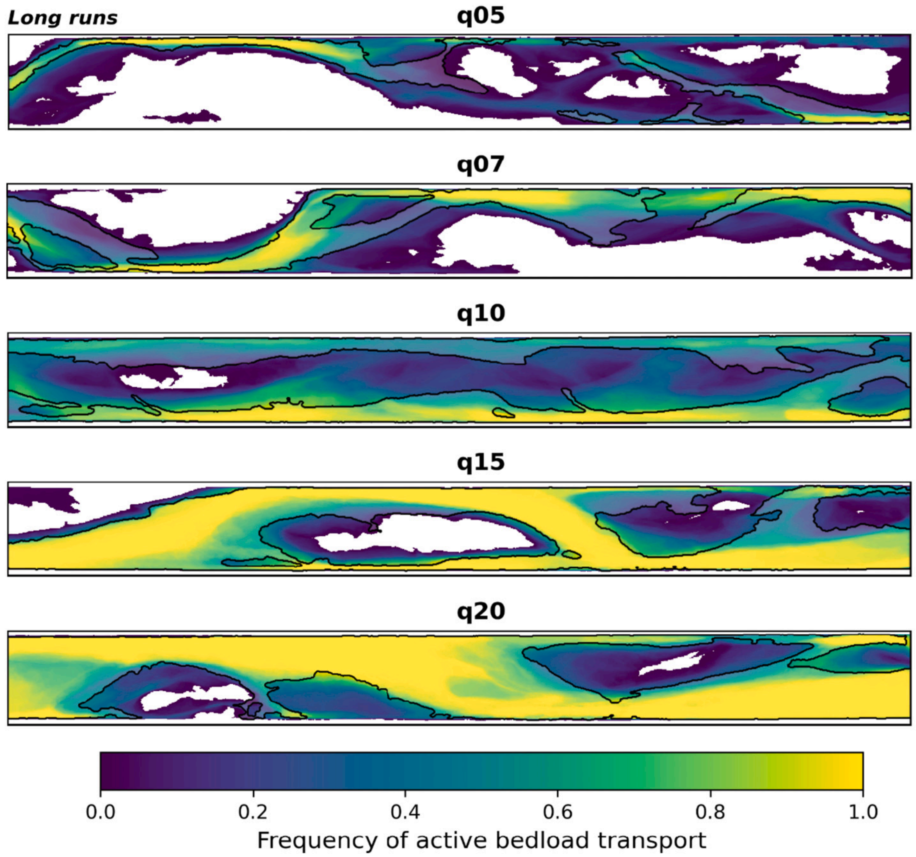

Fig. 5. Frequency maps of the instantaneous bedload transport of each long-run experiment. Black-contoured areas represent a snapshot of the instantaneous bedload transport activity.

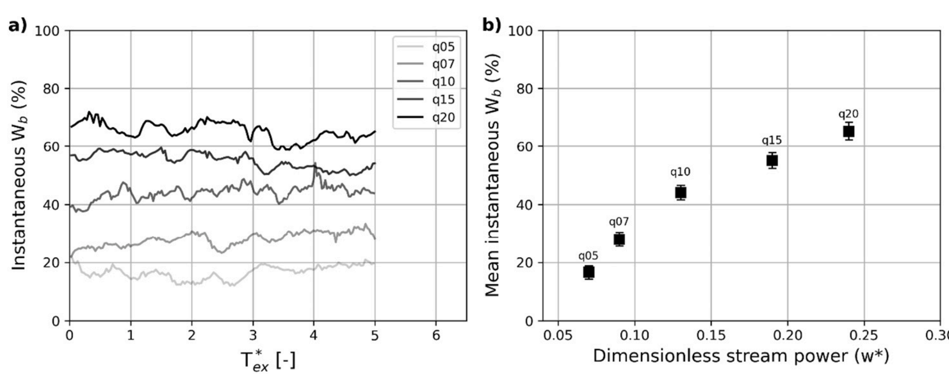

Fig. 6. Instantaneous bedload active width ratio W_b from long-runs of each experiment. a) Variability of W_b over five Exner timescale ratio duration T^*_{ex}. b) Mean W_b in function of dimensionless stream power.

short runs prevented us obtaining accurate results and therefore we excluded this dataset from the following analyses.

Results show that the variability of W_m remains low with a maximum standard deviation representing 15% of the mean W_m for the q05 experiment while the others are below 10%. The reach-scale morphological active width increases with dimensionless stream power from 27.8% ± 4.2% up to 47.3% ± 2.4% of the wetted width for the q05 and q20 experiments respectively. The q07 experiments, with a reach-scale W_m of 28.5% ± 2.7% exhibit a very similar morphological active width than the q05 experiment. The Exner time interval of measurement also varies with experiments and represents 0.46, 0.37, 0.34 and 0.56 of the Exner timescale T_{ex} for the q05, q07, q10 and q20 experiments respectively.

3.1.4. Bedload and morphological active widths across Exner time intervals

In this section, results of the bedload and morphological active width ratios over Exner time intervals from the short-run experiments are presented. Examples of both bedload transport activity and DoD maps are given for each experiment in Fig. 8.

The Exner time interval ΔT^*_{ex}spans an order of magnitude, ranging from 0.3 to 3.2 (Fig. 9). Both bedload and morphological active width ratios increase with ΔT^*_{ex}, with W_m consistently lower than W_b. The bedload active width ratio W_b increases from 80.1 ± 2.5% to 97 ± 0.0% for q20, 58.0 ± 3.0% to 81 ± 0.0% for q10, 43.0 ± 3.1% to 82 ± 0.0% for q07 and 36.7 ± 6.6% to 80.0 ± 0.0% for q05 experiments. The values of W_m are substantially lower and increase from 47.3 ± 2.4% to 67.8 ± 0.0% for q20, 35.2 ± 2.0% to 67.4 ± 0.0% for q10, 28.0 ± 2.6% to 69.5 ± 0.0% for q07 and 27.8 ± 4.2% to 66.2 ± 0.0% for q05

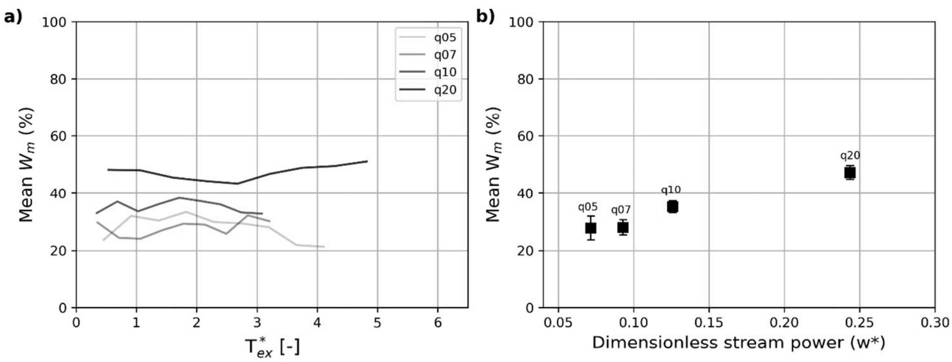

Fig. 7. Morphological active width W_m from short-run experiments. a) Variability of W_m in function of the Exner timescale ratio T^*_{ex}. b) Mean W_m in function of dimensionless stream power.

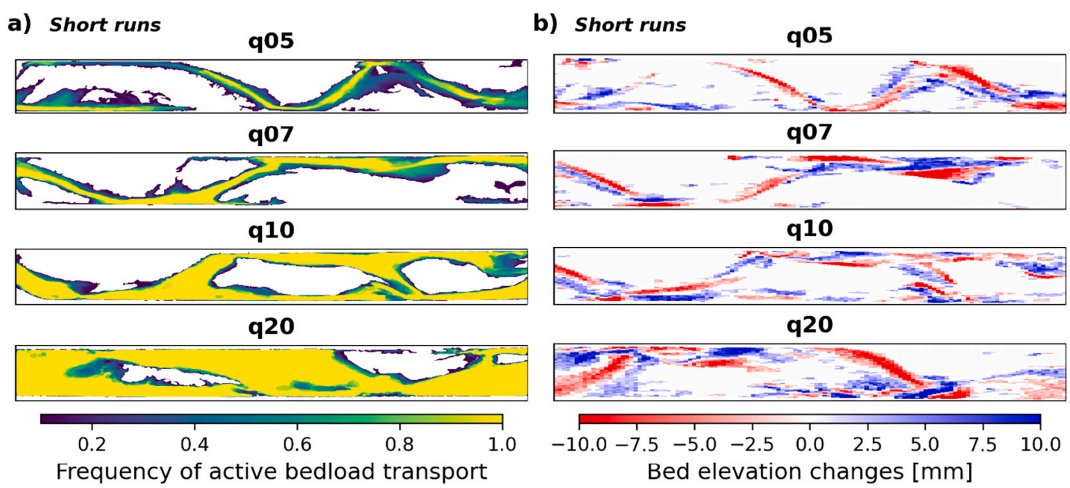

Fig. 8. Examples of bedload transport activity map and its resulted morphological imprint after one short run at the shortest Exner time interval survey frequency (0.4 ΔT_{ex}*). a) Frequency maps of the instantaneous bedload activity. b) Resulting morphological changes maps using DoD technique with DEMs before and after the run.

experiments.

A first observation in the mean difference between W_m and W_b is that it generally decreases with dimensionless stream power ω* regardless of the Exner time interval. At the shortest Exner time interval (i.e., around 0.3), the absolute mean difference in active width ratios is decreasing with dimensionless stream power ω* from 32.8 ± 4.5% to 8.9 ± 5.1% for q20 and q05 respectively (Fig. 10). For a similar ω* the mean difference remains roughly constant with a slight increase toward shorter ΔT^*_{ex} for the q10 experiment and a slight decrease for the q05 experiment. Moreover, W_m never reaches the same value of W_b regardless of ω* and ΔT^*_{ex}. Another observation is that W_m *is* already lower than the instantaneous W_b for the q20 (−18.0 ± 3.9%) and q10 experiments (−8.9 ± 3.3%), is equal for the q07 experiment (0.0 ± 3.7%), while it is higher for the q05 experiment (11.2 ± 4.8%) when considering the shortest ΔT_{ex}* for topographic surveys.

3.2. Morphological active width of the Tagliamento, Rees and Sunwapta rivers across Exner time intervals

This section presents the analysis of the morphological active width W_m from field data within the framework of the Exner timescale. Morphological active width ratios were derived from available Digital Elevation Model of Difference (DoD) datasets and cross-section differences. Each DoD results from a different Exner time interval (ΔT_{ex}*) between topographic surveys. Examples of DoD for Pinzano and Rees sites can be found in the Supplementary material (Fig. S4). These field-based results are compared with those from laboratory experiments (Fig. 11a). Additionally, Fig. 11b illustrates the range of Exner time intervals as a function of the return interval (i.e. magnitude) of flood events derived from the Tagliamento River flow record.

An initial observation is that the mean ΔT_{ex}* for the different field surveys ranges from 0.14 to 8.40 (Fig. 11a) with a mean dimensionless stream power ω^* of 0.16, 0.16, and 0.05 for the Rees, the Tagliamento and the Sunwapta rivers respectively. On average, the uncertainty on ΔT_{ex}* represents 68.6 ± 37.6%, 22.5 ± 9.7% and 56.0 ± 21.0% respectively. The relationship between W_m and ΔT_{ex}* for the Rees, Tagliamento, and Sunwapta Rivers show a similar trend than the one observed from the laboratory dataset with a Pearson correlation coefficient *r* of 0.93, 0.82 and 0.99 respectively, though with notable variability relative to corresponding dimensionless stream powers. In addition, the morphological active widths measured on the Sunwapta river are significantly lower for the same time interval than for the Rees and the Tagliamento exhibiting higher dimensionless stream power.

The results also show that the mean Exner timescale interval associated with return intervals of sediment transport events between 1 and 25 years falls within the laboratory range of 0.14 to 3.7 ΔT_{ex}* (Fig. 11b). Below a return interval of 5 years, the variability in ΔT_{ex}* is particularly high, spanning nearly the entire observed range. Furthermore, the higher is the transport event duration the higher is the ΔT_{ex}* highlighting that flood duration plays a more significant role than flood magnitude in determining the Exner timescale interval.

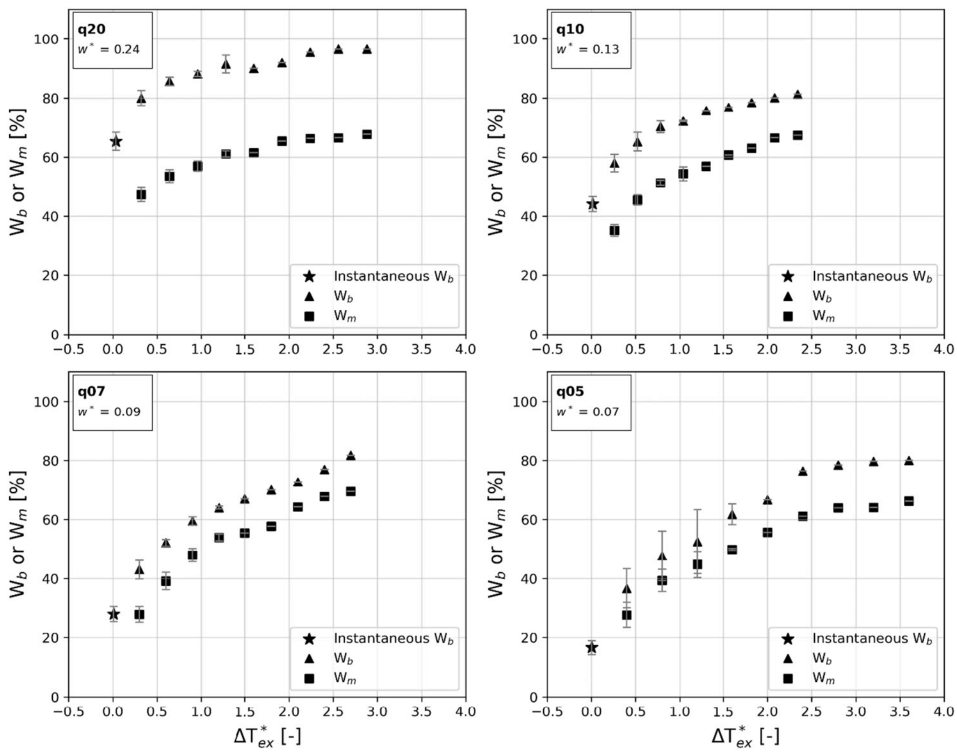

Fig. 9. Bedload and morphological active widths in function of survey time intervals ΔT_{ex}* for each set of short-run experiments. The instantaneous W_b is represented by a star symbol.

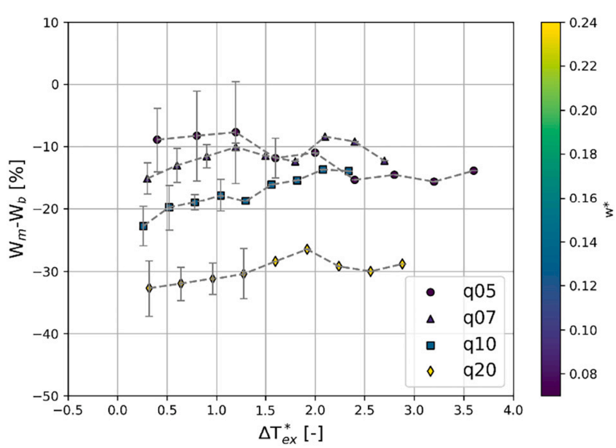

Fig. 10. Mean difference between the reach-averaged morphological and bedload active width W_b in function of the Exner time interval ΔT_{ex}* for each short-run experiments.

4. Discussion

4.1. The instantaneous bedload activity and active width compared to previous studies

The mapping of instantaneous bedload transport activity obtained through the time-lapse surveys highlights interesting patterns and processes, particularly how they evolve with decreasing formative discharge, resulting in a shift from a wandering to a braided configuration. As previously observed in flume experiments (Ashmore, 1991, 2001, 2013; Ashmore et al., 2011), braided morphologies are often characterized by a relatively small number of simultaneously active branches. The multi-thread pattern becomes more evident only when transport processes are observed over longer time scales. Data presented in.

Fig. 9 for experiments q05 and q07 show an approximately threefold increase in the bedload active width when the observation time interval is extended to three times the Exner time scale. This suggests significant lateral movement and/or planform displacement of the active width, confirming the high dynamics of braided morphologies. Flume width likely constrains these observations, particularly at longer timescales, implying that the observed threefold increase in active width represents a lower bound, as wider flumes would allow greater lateral channel mobility. However, the response would also depend on the spatio-temporal distribution of shear stress, making the resulting behaviour difficult to predict. Further experiments with larger flume widths are needed to investigate their effect on this observation.

The instantaneous active widths, calculated in this study using an objective and reproducible method, were compared with the values obtained by Garcia Lugo et al. (2015) based on visual inspection, as a function of dimensionless stream power (Fig. 12). Both approaches show similar trends for wandering and braided morphologies, consistent with other flume and field-based observations in gravel-bed rivers (Lisle et al., 2000; Haschenburger, 2006; Ashmore et al., 2011). Additionally, the results from this study extend the observed range of instantaneous bedload active widths to lower values of dimensionless stream power compared to the findings of Garcia Lugo et al. (2015), indicating that the almost linear trend continues down to a dimensionless stream power of 0.07. In the q05 experiment, we observed and measured significant bedload transport, differently from what was observed by Peirce et al. (2018), who reported a stream power threshold of 0.09 for bedload activity in their flume studies. This difference may be attributed to the nearly uniform grain size distribution in our experiments, likely reducing spatial variability in critical shear stress by limiting hiding–exposure effects, bed patchiness, and armoring, which are known to broaden mobility thresholds in gravel bed rivers (Recking et al., 2012; Smith et al., 2023). As a result, bedload transport initiation in our experiments can occur at lower dimensionless stream power than reported in flumes or field settings with mixed sediment. Data from the

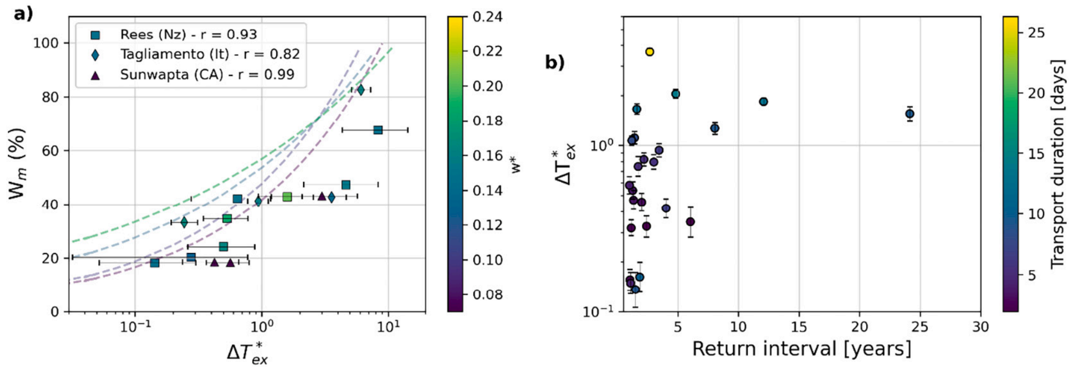

Fig. 11. a) Morphological active width W_m as a function of the survey time interval ΔT_{ex}* for the Tagliamento, Rees and Sunwapta river surveys. Dashed lines represent the power law fits from the lab experiment dataset. b) Flood return interval vs normalized flood duration ΔT_{ex}* for the Tagliamento River. Data to compute the return interval are from the Venzone hydrometric station for the period 1996–2024.

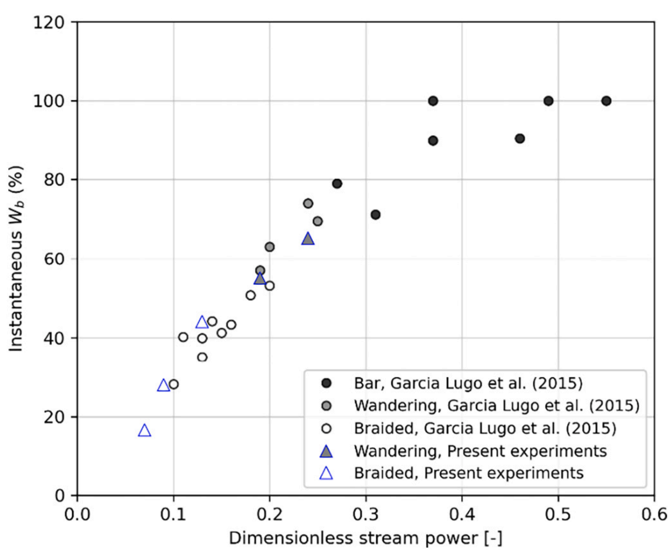

Fig. 12. The instantaneous bedload active width W_b of the present experiments with the Garcia Lugo et al. (2015) data vs dimensionless stream power. The instantaneous W_b values from Garcia Lugo et al. (2015) were estimated from visual inspections during each experiment.

three field case studies indicate that morphological change can be detected at dimensionless stream power values larger than approximately 0.1–0.12. Direct observations of the bedload active width in the field remain challenging due to water turbidity during floods, which hinders visual detection of bedload transport. The use of scour chains, particularly when combined with pebble tracking (RFID) technology and/or geophone sensors (Haschenburger and Church, 1998; Liébault and Laronne, 2008; Brenna et al., 2019), may provide useful information, although limited in their spatial extent. In this context, laboratory experiments remain a valuable tool for obtaining spatially and temporally accurate dataset of bedload transport.

4.2. On the discrepancy between bedload and morphological active widths

Our experiments highlighted a significant difference between the bedload active width ratio W_b and the morphological active ratio W_m across all investigated configurations. This discrepancy was particularly pronounced under conditions of higher discharge or stream power per unit width, i.e., when the flow was more constrained by the banks and had reduced lateral mobility. In all cases, the morphological active width was consistently lower than the bedload active width, indicating the occurrence of bedload transport not associated with detectable morphological change. This can result from several processes: i) morphological changes may have occurred but were too small to be captured by the differencing of digital elevation models; ii) compensation between scour and deposition may have taken place, where a sequence of erosion and deposition of similar magnitude results in no net morphological change (Lindsay and Ashmore, 2002); and iii) equilibrium (non-morphological) transport, wherein bedload moves through a short reach without altering bed morphology due to local equilibrium and the absence of spatial gradients in transport (Booker and Eaton, 2022).

Further analysis is needed to disentangle the relative contributions of these processes. Notably, we estimate that the detection limit of the DoD played a minor role overall since it is close to the grain size (1.3 mm). Moreover, the frequency distribution of elevation difference values *dZ* in areas of bedload transport without detected morphological changes is similar to the area with no transport (i.e. noise) for the lowest discharge (section S5 in the Supplementary materials). Compensation and equilibrium transport are both more likely to occur when lateral channel mobility is constrained, forcing the flow to repeatedly rework the same bed area. However, even the q05 and q07 experiments, which were characterized by a braided configuration, exhibited a significant difference between W_b and W_m, regardless of the time interval considered.

To quantify the spatial agreement between bedload activity and morphological change, we introduce a Spatial Concordance Index (SCI). The SCI is defined, for each pixel, as the proportion of instances in which both bedload transport and morphological change were observed, considering all nine short runs of a given experiment (Fig. 13). A SCI value of 0 indicates that morphological changes were never detected where bedload transport occurred, while a SCI of 1 signifies that morphological changes were always observed in conjunction with bedload activity at that pixel. In all experiments, regions with very low SCI values are typically located near the edges of the active area, potentially suggesting either limited bedload flux, or issues with morphological change detection. However, each experiment also displays areas of relatively low SCI values associated with high bedload frequency and located within the main active channel. This pattern is particularly pronounced in experiments with a higher discharge. For instance, in experiment q20, a major channel occupying approximately half the width of the flume, exhibited persistent bedload transport across all short runs. Nonetheless, large sections of this channel display SCI values between 0.4 and 0.6, indicating that in nearly half of the runs, no morphological change was detected despite ongoing bedload transport.

These findings suggest that in wandering/transitional systems (q15 and q20 experiments), 25–30% of total bedload transport may originate from equilibrium bedload transport or compensation in bed elevation changes leading to net zero changes as they are mainly located where most of the transport happens. However, in braided systems (q07 and q05 experiments), the proportion of equilibrium bedload transport and

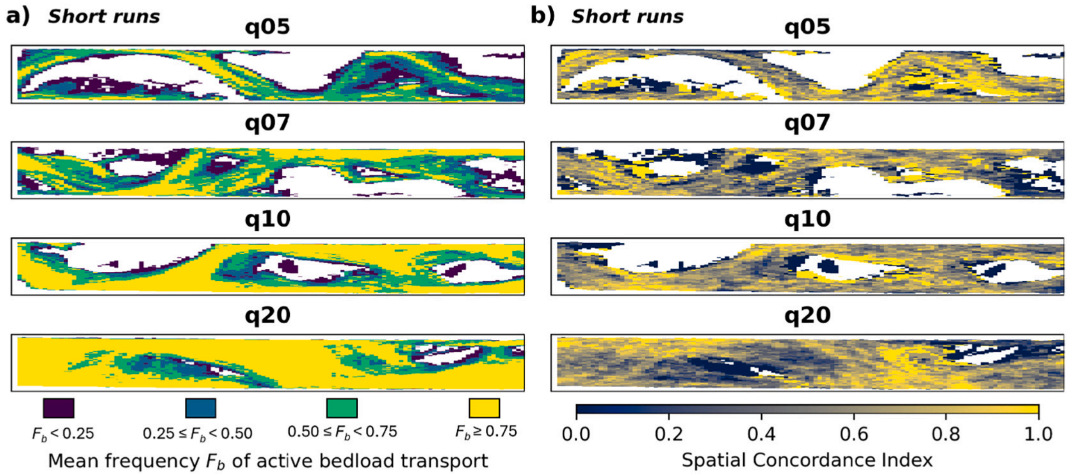

Fig. 13. Frequency maps of bedload transport (a) and spatial concordance index of the associated morphological changes (b) for each short run experiments at around 0.3 T_{ex} time intervals.

compensation effect clearly decline to 13–18% of bedload transport. These results demonstrate that even in braided systems a relatively small proportion of bedload transport cannot be observed and quantified from a morphological approach. It is important to note that the high degree of the bank-constrained wetted width in these experiments (>84% of the corridor width) is likely to play a role in the proportion of both equilibrium and compensation that are present. In addition, the constant sediment supply imposed here suppresses supply-driven bar growth and aggradation, which are key drivers of single-thread to braided transitions in gravel-bed rivers (Mueller and Pitlick, 2014). Under these conditions, channel adjustment and braiding initiation are primarily controlled by local hydraulics and geometry, promoting equilibrium transport and compensation effects that contribute to the observed mismatch between bedload transport and detectable morphological change for high discharges. Future experiments in larger settings and variable sediment supply are needed to further extend these results.

4.3. Effect of the time interval between surveys on active widths and the Exner timescale framework

In all experiments conducted, both bedload and morphological active width ratios increase with the Exner time interval. This observation underscores the critical role of the time interval between surveys and highlights the need to properly quantify it. In field settings, the time interval is linked to flood duration and to the technical limitations of surveying the riverbed during low-flow conditions. Longer floods are more likely to result in more extensive morphological changes, not only due to a longer time interval between surveys but also due to their potentially greater magnitude. It is also important to note that the absolute difference between W_m and W_b remains roughly constant across Exner time interval and thus W_m never reaches the same value as W_b for a given observation time interval, regardless of whether the morphology is wandering or braided. This indicates that non-morphological bedload transport occurs relatively consistently across a wide range of time intervals, at least within the morphological configurations explored in our experiments. Further experiments in wider settings, and therefore with lower bank-constrained flow width, are needed to extend these observations.

In braided rivers, it has been suggested that the morphological active width may approximate the instantaneous bedload active width at sufficiently short time intervals (Ashmore and Church, 1998; Lindsay and Ashmore, 2002). Results from the present experiments seem to support this statement. In wandering morphologies (e.g., q20 and q15), increasing the survey frequency does not result in a closer match between W_m and W_b. In more braided configurations, such as in experiments q07 and q05, the difference between W_m and W_b is reduced. For example, in q07 experiment the instantaneous W_b is comparable to W_m at ΔT_{ex}* equal to 0.3. In the q05 experiment, a time interval of approximately 0.4 T_{ex} is sufficient for W_m to exceed the instantaneous W_b (Fig. 9). Considering that the morphological active width requires a sufficiently long-time interval between surveys to capture significant morphological changes, it may be reasonable to consider W_m, when estimated at the shortest feasible time interval, as an acceptable proxy for the instantaneous W_b. However, this assumption may not hold if both are assessed over strictly equivalent time scales after integration across time.

The relevance of the time interval between surveys suggests the importance of correctly defining a normalized timescale to enable comparisons across different conditions and case studies. Results presented in Fig. 11 show that the proposed Exner timescale offers a suitable framework. Despite differences in longitudinal slope, grain size, formative discharge, and flood duration, the three case studies exhibit the same trend as the experimental data when compared using the normalized time interval. The effect of the dimensionless stream power in discriminating the W_m-ΔT_{ex}^* relationships is less pronounced than in the experimental data and requires further investigation.

Given the range of input parameter values (Table 1), uncertainties in the estimation of ΔT_{ex}* are primarily associated with the critical discharge Q_c. This parameter accounts for 89 ± 5%, 68 ± 18% and 64 ± 5% of the uncertainty for the Rees, the Tagliamento and the Sunwapta rivers respectively. This dominance arises because more than 87% of the discharge measurements at all study sites are below Q_c. For example, reducing Q_c from 30 m^3/s to 20 m^3/s for the Rees River increases the number of days exceeding Q_c by 81, resulting in a higher ΔT_{ex}*. This highlights the critical role of accurately estimating Q_c in determining ΔT_{ex}*. The second main source of uncertainty relates to the quantification of the sediment flux as a function of the water discharge. It is not common to have accurate field measurements at a range of discharges and therefore it is likely the estimate must be based on numerical modelling, imposing a transport capacity equation to compute the sediment flux. Accurate measurements of grain size distribution and or sediment flux and its spatio-temporal variability are needed to better estimate the related uncertainty on ΔT_{ex}* (Recking et al., 2024). The other hydraulic parameters (water depth and wetted width) are generally more easily estimated, from direct observations or, also in this case, from numerical modelling.

Values of ΔT_{ex}* estimated in the three case studies cover a range of more than one order of magnitude, from approximately 0.1 to 8 and they are related to floods of significantly different magnitude, from small, frequent flow pulses to major floods with return interval larger than 10 years. This confirms that the values chosen in the design of the laboratory experiments are meaningful and that the observations on bedload and morphological activity can be used to interpret the morphological evolution of gravel bed rivers.

5. Conclusion

In this study, we aimed at investigating the response in both bedload and morphological active widths to flood magnitude and duration, river morphology and time intervals between survey acquisitions. Our approach was to design flume experiments where both instantaneous bedload transport activity and the resulting morphological change can be mapped with a high spatio-temporal resolution. In that sense, this study provides the first attempt in describing the instantaneous bedload active width, from an objective and semi-automatic method, and to present direct comparison between time-integrated bedload and morphological active widths. Three different river morphologies were reproduced in the lab: alternate bars, wandering and braided river types. We choose to design the experiment duration and analyze the results under the Exner timescale framework aiming to reproduce a similar timescale for morphological evolution of the river bed across different flow conditions (Fujita, 1989; Garcia Lugo et al., 2015). Experimental results were compared with field data from three braided systems: the Tagliamento (IT), the Rees (NZ) and the Sunwapta (CA) rivers. The main findings can be summarized as follows:

1. The characterization of instantaneous bedload active width across different river morphologies confirms a strong positive correlation with dimensionless stream power, extending the established trend to lower values (~0.07; Fig. 12), in agreement with and expanding upon previous flume studies. In braided systems, bedload active width ranges from 16.6% to 44% of the wetted width, while in wandering systems with over 80% bank-constrained flow width, it exceeds 50%. These values were obtained using an objective, reproducible time-lapse imagery method, which proved effective in capturing bedload transport patterns and matched previous visual observations (Garcia Lugo et al., 2015). In braided rivers, extending the time interval of observation to values larger than one time the Exner timescale revealed a threefold increase in bedload active width, highlighting significant planform reworking and lateral mobility, and confirming the high dynamics of braided morphologies. These findings underscore the critical role of temporal scale in capturing the full extent of transport activity and sediment dynamics.
2. For all investigated river morphologies and time intervals of observation, the morphological active width is consistently lower than the bedload active width. However, this difference decreases with decreasing dimensionless stream power and along the morphological gradient from alternate bars to wandering and braided systems, dropping from approximately 33% to 9%, respectively. For a given morphology, the difference remains consistent across different observation intervals. Our analysis shows that this discrepancy is primarily due to compensation or equilibrium transport processes, which account for 25–30% of the total bedload transport area in alternate bar and wandering morphologies, and 13–18% in braided systems. These findings demonstrate that even in braided rivers, a portion of bedload transport is not captured through morphological change alone. It is important to note that the high degree of bank-constrained flow width in these experiments (>84% of the flume width) likely influenced the extent of compensation and equilibrium processes observed. These experiments also confirm that, for braided systems, the morphological active width can be considered as a good proxy for instantaneous bedload active width if estimated at sufficiently short time-interval. Further experiments in larger, less bank-constrained flow width settings are needed to validate and generalize these results.
3. The Exner timescale framework has proven to be a valuable tool for linking sediment transport dynamics to flood characteristics and for describing the morphological evolution of river systems. The timescales derived from laboratory experiments were consistent with field observations, reinforcing the applicability of flume-based approaches for studying sediment dynamics. This consistency supports the use of the Exner framework to compare results across different conditions and case studies, contributing to a broader understanding of gravel-bed river morphodynamics.

This study provides the first quantification of the difference between bedload and morphological active widths, thereby improving our understanding of one source of uncertainty in sediment flux estimation. These results also contribute to the interpretation of field data resulting from the morphological approach. Future studies should look at less bank-constrained flow conditions and a more intensely braiding system to expand the results presented in this paper.

CRediT authorship contribution statement

Thomas G. Bernard: Writing – original draft, Visualization, Software, Methodology, Investigation, Formal analysis, Data curation, Conceptualization. **Enrico Pandrin:** Writing – review & editing, Software, Methodology, Formal analysis, Data curation, Conceptualization. **Lindsay Capito:** Writing – review & editing, Methodology, Data curation. **Simone Bizzi:** Writing – review & editing, Supervision, Resources, Project administration, Funding acquisition, Conceptualization. **Walter Bertoldi:** Writing – review & editing, Validation, Supervision, Resources, Project administration, Methodology, Funding acquisition, Conceptualization.

Declaration of competing interest

The authors declare that they have no known competing financial interests or personal relationships that could have appeared to influence the work reported in this paper.

Acknowledgements

This work was supported by the PRIN project NextGenerationEU PRIN 2022 Prot. N. 20223RXTHB – RIVER WATCHING. The authors would like to thank Lorenzo Forti and Andrea Bampi (Hydraulic Laboratory at University of Trento) and Stefano Castelli (University of Padova) for their support with the experiments and Tagliamento field data acquisition.

Appendix A. Supplementary data

Supplementary data to this article can be found online at https://doi.org/10.1016/j.geomorph.2026.110229.

Data availability

DEMs and sediment fluxes from the lab q07, q10, q15 and q20 experiments are available here (Pandrin and Bertoldi, 2023): https://zenodo.org/records/8014454. DEMs for the q05 experiment and bedload transport activity maps for all experiments are available here: doi:https://doi.org/10.5281/zenodo.17018603.

References

Ancey, C., 2020a. Bedload transport: a walk between randomness and determinism. Part 1. The state of the art. J. Hydraul. Res. 58, 1–17. https://doi.org/10.1080/00221686.2019.1702594.

Ancey, C., 2020b. Bedload transport: a walk between randomness and determinism. Part 2. Challenges and prospects. J. Hydraul. Res. 58, 18–33. https://doi.org/10.1080/00221686.2019.1702595.

Ashmore, P., 1991. How do gravel-bed rivers braid? Can. J. Earth Sci. 28, 326–341. https://doi.org/10.1139/e91-030.

Ashmore, P., 2001. Braiding phenomena: statics and kinetics. In: Gravel Bed Rivers V, pp. 95–121.

Ashmore, P., 2013. 9.17 morphology and dynamics of braided rivers. In: Treatise on Geomorphology. Elsevier, pp. 289–312. https://doi.org/10.1016/B978-0-12-374739-6.00242-6.

Ashmore, P., Church, M., 1998. Sediment transport and river morphology: a paradigm for study. Gravel Bed Rivers Environ. 345, 115–139.

Ashmore, P., Bertoldi, W., Tobias Gardner, J., 2011. Active width of gravel-bed braided rivers. Earth Surf. Process. Landf. 36, 1510–1521. https://doi.org/10.1002/esp.2182.

Bakker, M., Antoniazza, G., Odermatt, E., Lane, S.N., 2019. Morphological response of an Alpine braided reach to sediment-laden flow events. Case Rep. Med. 124, 1310–1328. https://doi.org/10.1029/2018JF004811.

Belletti, B., Dufour, S., Piégay, H., 2015. What is the relative effect of space and time to explain the braided river width and island patterns at a regional scale?: braided river pattern at regional scale. River Res. Appl. 31, 1–15. https://doi.org/10.1002/rra.2714.

Bertoldi, W., Ashmore, P., Tubino, M., 2009a. A method for estimating the mean bed load flux in braided rivers. Geomorphology 103, 330–340. https://doi.org/10.1016/j.geomorph.2008.06.014.

Bertoldi, W., Zanoni, L., Tubino, M., 2009b. Planform dynamics of braided streams. Earth Surf. Process. Landf. 34, 547–557. https://doi.org/10.1002/esp.1755.

Bertoldi, W., Zanoni, L., Tubino, M., 2010. Assessment of morphological changes induced by flow and flood pulses in a gravel bed braided river: the Tagliamento River (Italy). Geomorphology 114, 348–360. https://doi.org/10.1016/j.geomorph.2009.07.017.

Bertoldi, W., Gurnell, A.M., Drake, N.A., 2011. The topographic signature of vegetation development along a braided river: results of a combined analysis of airborne lidar, color air photographs, and ground measurements. Water Resour. Res. 47, 2010WR010319. https://doi.org/10.1029/2010WR010319.

Booker, W.H., Eaton, B.C., 2022. Morphodynamic styles: characterising the behaviour of gravel-bed rivers using a novel, quantitative index. Earth Surf. Dyn. 10, 247–260. https://doi.org/10.5194/esurf-10-247-2022.

Bradski, G., 2000. The opencv library. Dr Dobbs J. Softw. Tools Prof. Program. 25, 120–123.

Brasington, J., 2010. From grain to floodplain: hyperscale models of braided rivers. J. Hydraul. Res. 48, 52–53.

Brenna, A., Surian, N., Mao, L., 2019. Virtual velocity approach for estimating bed material transport in gravel-bed rivers: key factors and significance. Water Resour. Res. 55, 1651–1674. https://doi.org/10.1029/2018WR023556.

Brasington, J., Vericat, D., Rychkov, I., 2012. Modeling river bed morphology, roughness, and surface sedimentology using high resolution terrestrial laser scanning. Water Resour. Res. 48, 2012WR012223. https://doi.org/10.1029/2012WR012223.

Brenna, A., Bizzi, S., Surian, N., 2022. A width-based approach to estimating historical changes in coarse sediment fluxes at river reach and network scales. Earth Surf. Process. Landf. 47, 2560–2579. https://doi.org/10.1002/esp.5395.

Capito, L., 2024. Bridging Morphological Scales in Sediment Transport: Path Length Estimation From Flume Experiments to Network-scale Sediment Transport Model Validation. Università degli Studi di Padova.

Capito, L.M., Pandrin, E., Bertoldi, W., Surian, N., Bizzi, S., 2024. Path length and sediment transport estimation from DEMs of difference: a signal processing approach. Earth Surf. Dyn. 12, 321–345. https://doi.org/10.5194/esurf-12-321-2024.

Davoren, A., Mosley, M.P., 1986. Observations of bedload movement, bar development and sediment supply in the braided Ohau river. Earth Surf. Process. Landf. 11, 643–652. https://doi.org/10.1002/esp.3290110607.

Egozi, R., Ashmore, P., 2009. Experimental analysis of braided channel pattern response to increased discharge. J. Geophys. Res. Earth Surf. 114, 2008JF001099. https://doi.org/10.1029/2008JF001099.

Exner, F.M., 1925. Über die Wechselwirkung zwischen Wasser und Geschiebe in Flüssen (On the interaction between water and sediment in streams). Akad Wiss Wien Math Naturwiss Kl 134, 165.

Ferguson, R.I., Ashmore, P.E., Ashworth, P.J., Paola, C., Prestegaard, K.L., 1992. Measurements in a Braided River chute and lobe: 1. Flow pattern, sediment transport, and channel change. Water Resour. Res. 28, 1877–1886. https://doi.org/10.1029/92WR00700.

Fujita, Y., 1989. Bar and channel formation in braided streams. In: Ikeda, S., Parker, G. (Eds.), Water Resources Monograph. American Geophysical Union, Washington, D. C., pp. 417–462. https://doi.org/10.1029/WM012p0417

Garcia Lugo, G.A., Bertoldi, W., Henshaw, A.J., Gurnell, A.M., 2015. The effect of lateral confinement on gravel bed river morphology: the effect of lateral confinement on river bed morphology. Water Resour. Res. 51, 7145–7158. https://doi.org/10.1002/2015WR017081.

Haschenburger, J.K., 2006. Observations of event-based streambed deformation in a gravel bed channel. Water Resour. Res. 42, 2006WR004985. https://doi.org/10.1029/2006WR004985.

Haschenburger, J.K., Church, M., 1998. Bed material transport estimated from the virtual velocity of sediment. Earth Surf. Process. Landf. 23, 791–808. https://doi.org/10.1002/(SICI)1096-9837(199809)23:9<791::AID-ESP888>3.0.CO;2-X.

Haschenburger, J.K., Wilcock, P.R., 2003. Partial transport in a natural gravel bed channel. Water Resour. Res. 39, 2002WR001532. https://doi.org/10.1029/2002WR001532.

Javernick, L., Redolfi, M., Bertoldi, W., 2018. Evaluation of a numerical model's ability to predict bed load transport observed in braided river experiments. Adv. Water Resour. 115, 207–218. https://doi.org/10.1016/j.advwatres.2018.03.012.

Legleiter, C.J., Roberts, D.A., Marcus, W.A., Fonstad, M.A., 2004. Passive optical remote sensing of river channel morphology and in-stream habitat: Physical basis and feasibility. Remote Sens. Environ. 93, 493–510. https://doi.org/10.1016/j.rse.2004.07.019.

Liébault, F., Laronne, J.B., 2008. Evaluation of bedload yield in gravel-bed rivers using scour chains and painted tracers: the case of the Esconavette Torrent (Southern French Prealps). Geodin. Acta 21, 23–34. https://doi.org/10.3166/ga.21.23-34.

Liébault, F., Piégay, H., 2002. Causes of 20th century channel narrowing in mountain and piedmont rivers of southeastern France. Earth Surf. Process. Landf. 27, 425–444. https://doi.org/10.1002/esp.328.

Lindsay, J.B., Ashmore, P.E., 2002. The effects of survey frequency on estimates of scour and fill in a braided river model. Earth Surf. Process. Landf. 27, 27–43. https://doi.org/10.1002/esp.282.

Lisle, T.E., Nelson, J.M., Pitlick, J., Madej, M.A., Barkett, B.L., 2000. Variability of bed mobility in natural, gravel-bed channels and adjustments to sediment load at local and reach scales. Water Resour. Res. 36, 3743–3755. https://doi.org/10.1029/2000WR900238.

Middleton, L., Ashmore, P., Leduc, P., Sjogren, D., 2019. Rates of planimetric change in a proglacial gravel-bed braided river: field measurement and physical modelling. Earth Surf. Process. Landf. 44, 752–765. https://doi.org/10.1002/esp.4528.

Mueller, E.R., Pitlick, J., 2014. Sediment supply and channel morphology in mountain river systems: 2. Single thread to braided transitions. Case Rep. Med. 119, 1516–1541. https://doi.org/10.1002/2013JF003045.

Pandrin, E., Bertoldi, W., 2023. DEMs and Sediment Flux From Pi Flume experiments. https://doi.org/10.5281/zenodo.8014453.

Parker, G., 1990. Surface-based bedload transport relation for gravel rivers. J. Hydraul. Res. 28, 417–436. https://doi.org/10.1080/00221689009499058.

Peirce, S., Ashmore, P., Leduc, P., 2018. The variability in the morphological active width: results from physical models of gravel-bed braided rivers. Earth Surf. Process. Landf. 43, 2371–2383. https://doi.org/10.1002/esp.4400.

Piégay, H., Arnaud, F., Belletti, B., Cassel, M., Marteau, B., Riquier, J., Rousson, C., Vazquez-Tarrio, D., 2023. Why consider geomorphology in river rehabilitation? Land 12, 1491. https://doi.org/10.3390/land12081491.

Powell, D.M., 2014. Flow resistance in gravel-bed rivers: progress in research. Earth Sci. Rev. 136, 301–338. https://doi.org/10.1016/j.earscirev.2014.06.001.

Recking, A., Liébault, F., Peteuil, C., Jolimet, T., 2012. Testing bedload transport equations with consideration of time scales. Earth Surf. Process. Landf. 37, 774–789. https://doi.org/10.1002/esp.3213.

Recking, A., Johannot, A., Horita, K., Nasr, M., Vázquez-Tarrío, D., Zanker, S., Fontaine, F., Melun, G., 2024. An attempt to take into account natural variability in 1D bedload prediction. Case Rep. Med. 129, e2023JF007601. https://doi.org/10.1029/2023JF007601.

Redolfi, M., 2014. Sediment Transport and Morphology of Braided Rivers: Steady and Unsteady Regime. University of Trento, Queen Mary University of London (PhD thesis).

Redolfi, M., Tubino, M., Bertoldi, W., Brasington, J., 2016. Analysis of reach-scale elevation distribution in braided rivers: definition of a new morphologic indicator and estimation of mean quantities. Water Resour. Res. 52, 5951–5970. https://doi.org/10.1002/2015WR017918.

Redolfi, M., Guidorizzi, L., Tubino, M., Bertoldi, W., 2017. Capturing the spatiotemporal variability of bedload transport: a time-lapse imagery technique. Earth Surf. Process. Landf. 42, 1140–1147. https://doi.org/10.1002/esp.4126.

Redolfi, M., Bertoldi, W., Tubino, M., Welber, M., 2018. Bed load variability and morphology of gravel bed rivers subject to unsteady flow: a laboratory investigation. Water Resour. Res. 54, 842–862. https://doi.org/10.1002/2017WR021143.

Smith, H.E.J., Monsalve, A.D., Turowski, J.M., Rickenmann, D., Yager, E.M., 2023. Controls of local grain size distribution, bed structure and flow conditions on sediment mobility. Earth Surf. Process. Landf. 48, 1990–2004. https://doi.org/10.1002/esp.5599.

Van Der Walt, S., Schönberger, J.L., Nunez-Iglesias, J., Boulogne, F., Warner, J.D., Yager, N., Gouillart, E., Yu, T., 2014. scikit-image: image processing in Python. PeerJ 2, e453. https://doi.org/10.7717/peerj.453.

Vázquez-Tarrío, D., Ruiz-Villanueva, V., Garrote, J., Benito, G., Calle, M., Lucía, A., Díez-Herrero, A., 2024. Effects of sediment transport on flood hazards: lessons learned and remaining challenges. Geomorphology 446, 108976. https://doi.org/10.1016/j.geomorph.2023.108976.

Virtanen, P., Gommers, R., Oliphant, T.E., Haberland, M., Reddy, T., Cournapeau, D., Burovski, E., Peterson, P., Weckesser, W., Bright, J., Van Der Walt, S.J., Brett, M., Wilson, J., Millman, K.J., Mayorov, N., Nelson, A.R.J., Jones, E., Kern, R., Larson, E., Carey, C.J., Polat, İ., Feng, Y., Moore, E.W., VanderPlas, J., Laxalde, D., Perktold, J., Cimrman, R., Henriksen, I., Quintero, E.A., Harris, C.R., Archibald, A.M., Ribeiro, A. H., Pedregosa, F., Van Mulbregt, P., SciPy 1.0 Contributors, Vijaykumar, A., Bardelli, A.P., Rothberg, A., Hilboll, A., Kloeckner, A., Scopatz, A., Lee, A., Rokem, A., Woods, C.N., Fulton, C., Masson, C., Häggström, C., Fitzgerald, C., Nicholson, D.A., Hagen, D.R., Pasechnik, D.V., Olivetti, E., Martin, E., Wieser, E., Silva, F., Lenders, F., Wilhelm, F., Young, G., Price, G.A., Ingold, G.-L., Allen, G.E., Lee, G.R., Audren, H., Probst, I., Dietrich, J.P., Silterra, J., Webber, J.T., Slavič, J., Nothman, J., Buchner, J., Kulick, J., Schönberger, J.L., De Miranda Cardoso, J.V., Reimer, J., Harrington, J., Rodríguez, J.L.C., Nunez-Iglesias, J., Kuczynski, J., Tritz, K., Thoma, M., Newville, M., Kümmerer, M., Bolingbroke, M., Tartre, M., Pak, M., Smith, N.J., Nowaczyk, N., Shebanov, N., Pavlyk, O., Brodtkorb, P.A., Lee, P., McGibbon, R.T., Feldbauer, R., Lewis, S., Tygier, S., Sievert, S., Vigna, S., Peterson, S., More, S., Pudlik, T., Oshima, T., Pingel, T.J., Robitaille, T.P., Spura, T.,

Jones, T.R., Cera, T., Leslie, T., Zito, T., Krauss, T., Upadhyay, U., Halchenko, Y.O., Vázquez-Baeza, Y., 2020. SciPy 1.0: fundamental algorithms for scientific computing in Python. Nat. Methods 17, 261–272. https://doi.org/10.1038/s41592-019-0686-2.
Wheaton, J.M., Brasington, J., Darby, S.E., Sear, D.A., 2010. Accounting for uncertainty in DEMs from repeat topographic surveys: improved sediment budgets. Earth Surf. Process. Landf. 35, 136–156. https://doi.org/10.1002/esp.1886.
Williams, Rust, 1969. The sedimentology of a braided river. J. Sediment. Res. 39, 649–679.
Williams, R.D., Brasington, J., Vericat, D., Hicks, D.M., 2014. Hyperscale terrain modelling of braided rivers: fusing mobile terrestrial laser scanning and optical bathymetric mapping. Earth Surf. Process. Landf. 39, 167–183. https://doi.org/10.1002/esp.3437.
Williams, R.D., Brasington, J., Hicks, D.M., 2016. Numerical modelling of braided river morphodynamics: review and future challenges. Geogr. Compass 10, 102–127. https://doi.org/10.1111/gec3.12260.
Wohl, E., Bledsoe, B.P., Jacobson, R.B., Poff, N.L., Rathburn, S.L., Walters, D.M., Wilcox, A.C., 2015. The natural sediment regime in rivers: broadening the foundation for ecosystem management. BioScience 65, 358–371. https://doi.org/10.1093/biosci/biv002.
Wohl, E., Fryirs, K., Grabowski, R.C., Morrison, R.R., Sear, D., 2024. Enhancing the natural absorbing capacity of rivers to restore their resilience. BioScience 74, 782–796. https://doi.org/10.1093/biosci/biae090.
Wong, M., Parker, G., 2006. Reanalysis and correction of bed-load relation of Meyer-Peter and Müller using their own database. J. Hydraul. Eng. 132, 1159–1168. https://doi.org/10.1061/(ASCE)0733-9429(2006)132:11(1159).